

Supporting Information for:

**Fluorescence-Encoded Infrared Vibrational
Spectroscopy with Single-Molecule Sensitivity**

Lukas Whaley-Mayda[†], Abhirup Guha[†], Samuel B. Penwell[†], and Andrei Tokmakoff^{†*}

[†]Department of Chemistry, James Franck Institute, and Institute for Biophysical
Dynamics, The University of Chicago, Illinois 60637, United States

^{*}Corresponding Author: Email: tokmakoff@uchicago.edu

Contents

1	Sample preparation and steady-state FTIR, UV/Vis absorption, and fluorescence spectra	2
2	Experimental details of FEIR instrumentation	2
3	Time-gated photon acquisition with TCSPC	4
4	FEIR-CS data acquisition and processing	7
5	Details of FEIR signal concentration dependence	11

1 Sample preparation and steady-state FTIR, UV/Vis absorption, and fluorescence spectra

Coumarin 6 (C6) was used as received from Acros Organics. Solutions for steady-state fluorescence (3 μM) and UV/vis absorption (40 μM) measurements were prepared in acetonitrile. For FTIR absorption a 2 mM solution in acetonitrile-d₃ was used to take advantage of higher solvent transparency.

The fluorescence emission spectrum was recorded with a Horiba Fluorolog 3 spectrometer using right-angle detection from a 1 cm pathlength cuvette. The UV/vis absorption spectrum was measured at 1 cm pathlength in a Cary 5000 UV-Vis-NIR spectrophotometer. The FTIR spectrum was collected in a Bruker Tensor 27 spectrometer with the solution held in a 500 μm pathlength demountable cell with Barium Fluoride windows (Spectral Systems). The spectrum in main text Figure 1c is solvent-subtracted.

Solutions used for all FEIR experiments, including the concentration dependence, were prepared in acetonitrile-d₃ by serial dilution.

2 Experimental details of FEIR instrumentation

The instrumentation used for the FEIR experiments performed here builds on the optical design described previously in Whaley-Mayda *et al.*,¹ with the key modification of a new, custom-built microscope used for IR and visible beam delivery and fluorescence detection. The new microscope design allows for higher IR throughput into the sample, simplified alignment and diagnostic capabilities, and higher fluorescence collection efficiency. The generation and characterization of femtosecond mid-IR and visible pulses from the 1 MHz fiber laser pump (Coherent Monaco 1035-40) via a home-built optical parametric amplifier (OPA) and frequency-doubling of the fundamental, respectively, is the same as in ref. 1. Likewise for the Mach-Zehnder interferometer used to produce IR pulse-pairs with controllable delay τ_{IR} . A second mechanical translation stage (AeroTech ANT95-50L-MP) was added in the visible line to allow for independent control of the τ_{enc} and τ_{IR} time-delays.

The FEIR microscope, shown schematically in main text Figure 1b, was constructed largely using components from the Thorlabs Cerna Series. The visible objective lens (Zeiss A-Plan 63x NA 0.8) and Zinc Selenide (ZnSe) aspheric lens (ISP Optics ASPH-ZC-25-12, NA \approx 0.7) used for focusing the visible and IR beams, respectively, are the same as used in ref. 1, and the characterization of their respective focal spots reported therein remains valid. The linearly polarized visible beam is routed through a $\lambda/2$ waveplate (Thorlabs WPH10M-514) to set the polarization relative to the IR beam in the sample (parallel polarization was used exclusively). A dichroic mirror (Semrock FF526-Di01) reflects the visible beam towards the sample and transmits the fluorescence, which is passed through a notch (Thorlabs NF-514-17) and bandpass (Semrock FF01-550/49) filter before being focused by a 150 mm focal length lens (Thorlabs AC254-150-A) onto a single-photon avalanche photodiode (SPAD, MPD PDM 50). This focal length was chosen to produce the magnification required to roughly match the image size of visible focus' airy disk (45.5 μm) with the active area of the detector (50 μm), thereby creating confocal conditions. The combined transmission spectrum of the dichroic, notch, and bandpass filters is shown in green in main text Figure 1d.

The estimate of 1% overall fluorescence collection efficiency cited in the main text is calculated by multiplying together estimates of the objective collection efficiency (10%), overlap of emission bandpass and fluorescence spectrum (21%), and detector quantum efficiency (45%).² The 10% objective collection efficiency is calculated via $\sin^2(\theta/2)$ for the acceptance half-angle $\theta = \arcsin(\text{NA}/n)$

in acetonitrile ($n = 1.34$).

Sample solutions were held in a home-built cell between a 175 μm thick glass coverslip (top, visible/fluorescence side) and 1 mm thick Calcium Fluoride (CaF_2) window (bottom, IR side) separated by a 50 μm thick Teflon spacer. The sample is mounted to three axes of translation (Thorlabs PLS-XY and ZFM2020) driven by a Thorlabs MCM3001 controller for positioning into the focus. The onset of thermal effects (described in detail in the SI of ref. 1) caused by the IR absorption of the poorly transparent glass coverslip limits the maximum IR power used in this work (constant in all FEIR experiments at 50 nJ pulse energy, 50 mW average power, 23 kW/cm^2 average focal intensity). However, we note that replacing the glass coverslip with a 200 μm thick CaF_2 window removes heating artifacts and allows for at least 50% higher IR powers (the maximum currently available from the OPA).

As described in ref. 1, FEIR data for 1-IR-pulse relaxation transients and Fourier transform spectra is acquired by continuously scanning the relevant delay stage and using a position-tracking waveform (position synchronized output (PSO)) derived from the stage controller (AeroTech A3200 Npaq) to assign photons to their respective delay bins on the fly. A scan speed of 2 mm/s was used for all FEIR measurements, which takes about 3-4 seconds per scan (both directions of travel) for the delay ranges used (τ_{enc} over -3 to 10 ps, τ_{IR} over -2 to 8 ps for 30 μM and 30 nM data, and -2 to 6 ps for 1 nM data). For the 30 μM data in Figures 1e, 1f, and 4d, multiple scans were accumulated over at most 5 minutes and averaged together. For the 1 and 30 nM data in Figures 4c and 4d, scans were accumulated for 30 minutes. The methods for processing time-domain FEIR data into a Fourier transform spectrum are described in ref. 1.

1-IR-pulse scans and the FEIR-CS measurements are performed with the IR pulse-pair set at zero delay ($\tau_{\text{IR}} = 0$). Doing so relies on maintaining interferometric stability of the relative pathlength between the arms of the Mach-Zehnder interferometer over the course of the measurement. Considering stability at the $\lambda/10$ level for the ~ 6 μm mid-IR wavelength used results in the requirement of resilience to pathlength fluctuations and drift on the order of 0.6 μm , which is readily met in practice.

3 Time-gated photon acquisition with TCSPC

Time-correlated single-photon counting (TCSPC) is performed using a PicoQuant Time-Harp 260 PICO PCIe card. The sync channel is provided by a delay generator (SRS DG645) triggered off the fiber laser amplifier. The photon channel is the 15dB attenuated NIM output of the SPAD. For FEIR measurements the PSO waveform from the delay stage controller is sent to the TCSPC card and used as a marker integrated into the time-tagged time-resolved (TTTR) photon record. This raw TTTR record is either processed on the fly by custom LabView code, or saved for analysis in post-processing. The result is two-dimensional data, where one dimension is the scanned optical delay (τ_{enc} or τ_{IR}), and the other is the photon arrival time relative to the sync channel (microtime) with 25 ps bins. The TCSPC instrument response function (IRF) was measured from visible pump light reflected from the air-coverslip interface with the spectrally-selective fluorescence filter-set replaced with appropriate neutral density filters.

Figure S1a shows the raw microtime-resolved count data from a 1-IR-pulse measurement on a 30 μm C6 solution. Here and in all other 1-IR-pulse scan data in this work the τ_{enc} bin size is 40 fs. Figure S1b shows the projection of this raw data onto the τ_{enc} axis (i.e. integration over microtime). Figure S1c shows the projection onto the microtime axis, producing a TCSPC histogram. To avoid distorting the microtime decay kinetics the maximum count rate (indicated on the right y-axis of Figure S1b) is kept below 5% of the repetition-rate.³ The IRF, shown in gray in Figure S1c, has a 250 ps FWHM with a more slowly relaxing tail for positive microtimes. The zero of microtime is set at the maximum of the IRF.

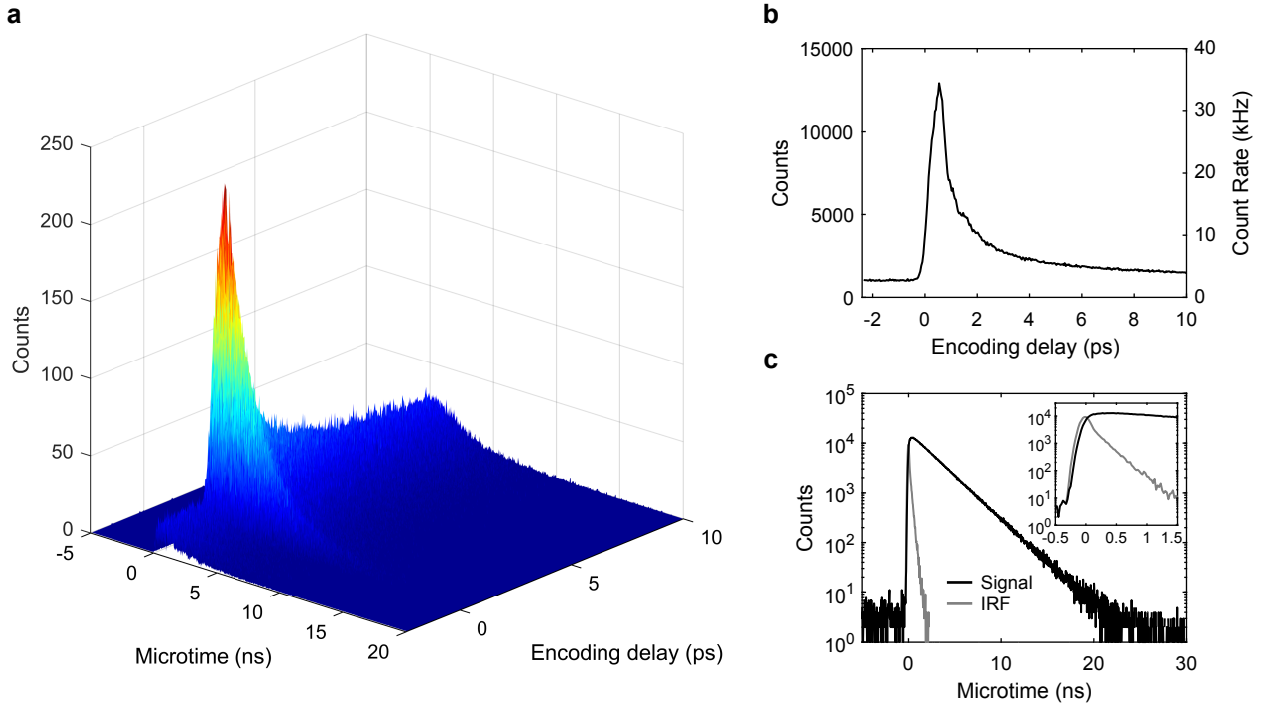


Figure S1: (a) Microtime-resolved photon count data for a 1-IR-pulse FEIR measurement on 30 μm C6. (b) Projection onto the τ_{enc} axis. (c) Projection onto the microtime axis (black), and the IRF (gray). Inset shows detail of the early time data.

As discussed in the main text, we time-gate the photon data based on microtime to remove scattering background. Figure S2a shows TCSPC histograms of every photon’s microtime from 1-IR-pulse FEIR measurements on C6 solutions at 30 μM , 30 nM, and 1 nM, along with the IRF. At the highest concentration the emission kinetics show a clean single-exponential decay with a 2.5 ns lifetime, indicating that the majority of detected photons are C6 fluorescence. At 30 nM a prompt component due to scattering that conforms to the shape of the IRF appears, and by 1 nM dominates the distribution. Due to the separation of timescales between the IRF duration and fluorescence lifetime, a substantial portion of this scattering component can be eliminated by only accepting photons within the time gate indicated by dashed lines in Figure S2a. As shown in Figure S2b, the resulting time-gated 1 nM FEIR transient has a 4-fold reduction in background and subsequently contends with less shot noise than the raw, un-gated data—at the expense of a 30% loss in FEIR signal counts. This gated 1 nM FEIR transient is shown in main text Figure 3c. The dependence of the FEIR signal F_1 , background $F_0 + B$, and modulation ratio $M = F_1/(F_0 + B)$ on the starting edge of the time gate (Figure S2c) demonstrates this tradeoff between improving signal to background and losing signal, with what we believe to be a roughly optimal compromise at 1 ns indicated. Figures S2d and S2e demonstrate the background-reducing effect of this time-gate on the 1-10 nM range of the C6 concentration dependence (un-gated data same as main text Figure 2). We note that time-gating offers minimal improvement for FEIR spectra, as the Fourier transform filters the background out with the DC component while its associated noise is distributed across the entire frequency axis, diluting its contribution within the IR pulse bandwidth.

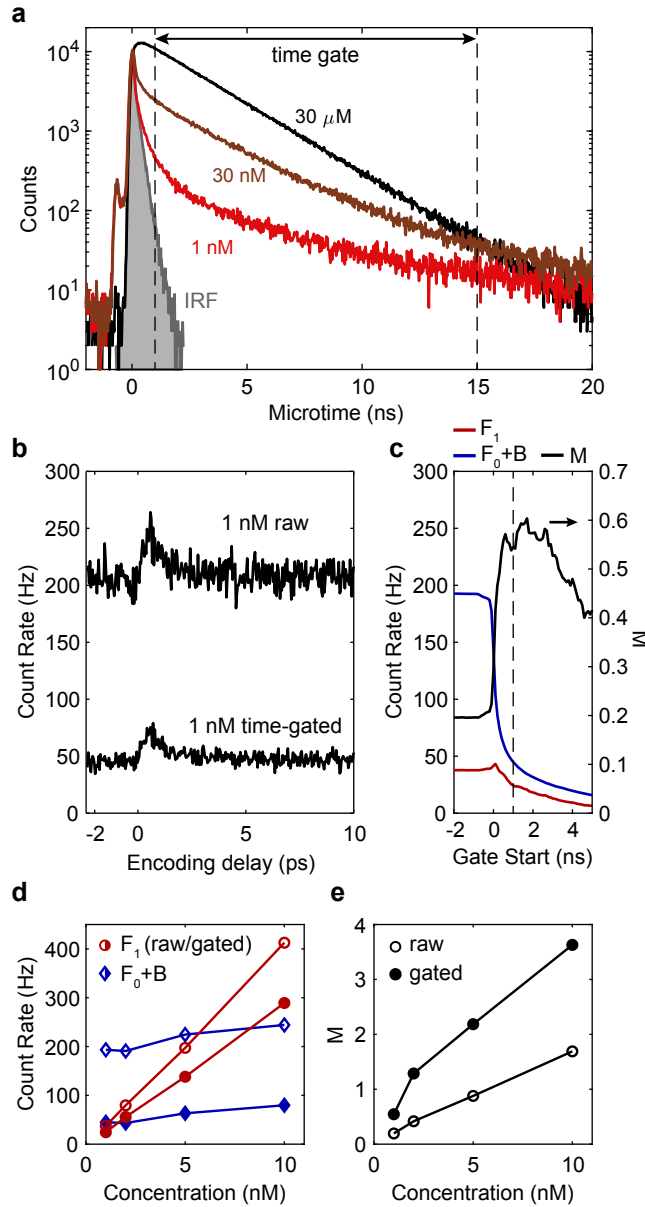


Figure S2: (a) TCSPC histograms from 1-IR-pulse FEIR measurements on C6 at $30 \mu\text{M}$ (black), 30 nM (brown), and 1 nM (red) with the IRF (gray). The time-gate (1 ns to 15 ns) used in panels (b), (d), and (e) is indicated by dashed black lines. (b) Comparison of raw and time-gated 1-IR-pulse FEIR measurements at 1 nM . (c) F_1 (red) and F_0+B (blue) count rates (left y-axis), and M (black, right y-axis) from the data in panel (b) as a function of the starting edge of the time gate with the ending edge fixed at 15 ns. The optimal starting edge at 1 ns is indicated by a dashed black line. (d) F_1 (red circles) and F_0+B (blue diamonds) count rates as a function of C6 concentration. Filled symbols are time-gated, open symbols are raw. (e) Modulation ratios corresponding to the count levels in panel (d). The visible pulse energy used for (b)-(e) and the 1 nM data in (a) was 12 pJ .

4 FEIR-CS data acquisition and processing

Raw photon time-series for FEIR-CS measurements are saved as TTTR records, and the correlation function is computed in post-processing by an algorithm described by Wahl *et al.*⁴ Time-series are recorded in 3 minute sections, and the resulting correlation functions are averaged together. Each FEIR-CS correlation function in main text Figure 3a was the result of a 60 minute total acquisition time. Prior to autocorrelation, the time-series are time-gated by microtime, which serves the purpose of removing the artifact caused by detector afterpulsing in addition to reducing scattering background as discussed above.

Figure S3 demonstrates the removal of the afterpulsing artifact using conventional FCS data from a 1 nM rhodamine 6G (R6G) solution in acetonitrile-d₃ as an example. R6G is directly resonant with the visible pulse, and the IR beam is not present. Figure S3a shows TCSPC histograms of the fluorescence signal with the IRF for reference. Afterpulses, caused by residual charge-carriers trapped after the primary photo-electron detection event, can be seen as the low-amplitude resurgence of counts after the hardware-fixed 75 ns dead-time. While rare ($< 0.2\%$ probability²), their high time-correlation with true photon counts leads to a prominent spike at early times in the correlation function (Figure S3b). If the afterpulsing temporal distribution function is well characterized, this artifact may be suppressed with a filtering algorithm.⁵ However, in our case the repetition-rate (1 MHz) is low enough that the afterpulse distribution fully decays before the next excitation pulse arrives, and therefore afterpulses can be explicitly excluded by only accepting photons for correlation that have microtimes shorter than the 75 ns dead-time. As shown in Figure S3b, gating photons in this way removes the afterpulsing spike, providing clean data all the way to the 1 μ s time-resolution limit (inverse of the repetition-rate).

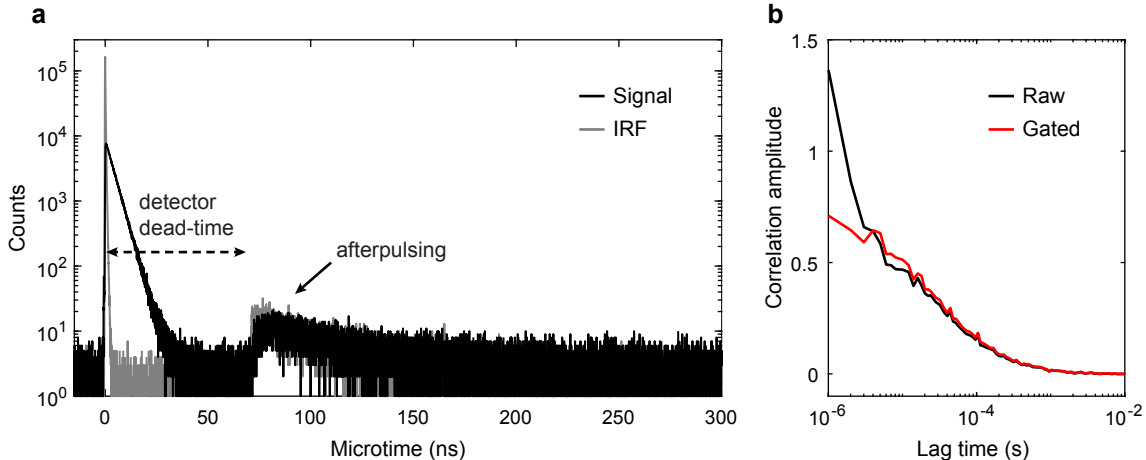


Figure S3: (a) TCSPC histograms of R6G fluorescence and the IRF. The full microtime axis has a range of roughly 819 ns, corresponding to the Time-Harp's 2^{15} bins of 25 ps width. (b) FCS correlation functions of the raw time series (all photons, black), and with only accepting photons with microtime < 30 ns (excluding afterpulses, red).

The FEIR-CS correlation functions

$$G(t) = \frac{\langle \delta F(0) \delta F(t) \rangle}{\langle F \rangle^2}, \quad (1)$$

where

$$\delta F(t) = F(t) - \langle F \rangle, \quad (2)$$

are fit by the following commonly used model function that assumes diffusion of a single species with diffusion constant D through a 3D ellipsoidal Gaussian probe volume⁶

$$G(t) = \frac{1}{\langle N \rangle} \left(1 + \frac{t}{\tau_D} \right)^{-1} \left(1 + \frac{t}{\kappa^2 \tau_D} \right)^{-1/2} \quad (3)$$

with $\tau_D = \frac{w_{xy}^2}{4D}$, $\kappa = \frac{w_z}{w_{xy}}$, and $\langle N \rangle = C\pi^{3/2}w_{xy}^2w_z$. The average molecule number $\langle N \rangle$ and diffusion timescale τ_D are fit parameters, and the probe volume aspect ratio $\kappa = \frac{w_z}{w_{xy}}$ (a rather insensitive parameter) is fixed at 4, the value estimated from the visible focal volume characterization in ref. 1. Estimates for the individual probe volume dimensions w_{xy} and w_z can be made based on that characterization, but are not required for the determination of $\langle N \rangle$. While w_{xy} and w_z connect the bulk concentration C to $\langle N \rangle$, the *definition* of $\langle N \rangle$ via the correlation amplitude (i.e. the average occupation number consistent with the Poisson fluctuation statistics) is a conceptually satisfying approach that is independent of the exact shape of the probe volume.

Uncorrelated background contributes to the denominator but not the numerator of $G(t)$ in Eq.1, thereby lowering its amplitude and artificially inflating the measured value of $\langle N \rangle$.^{7,8} Reducing the background from scattering by the time-gating method described above is therefore crucial for our FEIR-CS measurements. In general, time-gating or more sophisticated filtering methods using TCSPC can be applied to FCS measurements to improve accuracy or discriminate species by lifetime.^{9,10}

Figure S4a shows the effect of varying the starting edge of the time gate on the FEIR-CS correlation function measured from the 1 nM C6 sample (main text Figure 3a). The starting edges relative to the TCSPC histogram are depicted in Figure S4b with the same color-coding. The ending edge of the gate is fixed at 15 ns. As shown in Figure S4c, the early-time correlation amplitude $G(0)$ extracted from the fit increases dramatically as the starting edge is scanned over the prompt scattering component, and appears to reach a saturating value of 1.54 for edges > 2 ns. While other background sources with emission kinetics on the fluorescence timescale are likely still present, we take this value, corresponding to $\langle N \rangle = 0.65$ as our best estimate of the average molecule number. As evident in Figure S4a, the signal to noise degrades rapidly for increasingly aggressive time-gates as useful FEIR signal is thrown away, and we choose the 1 - 15 ns gate (cyan curve) as a compromise (used for all correlation functions in main text Figure 3a). The error bars on $\langle N \rangle$ in main text Figure 4b correspond to 95% confidence intervals from the fit routine.

The fit to the 1 nM FEIR-CS correlation function produces a diffusion time constant $\tau_D = 47 \pm 5 \mu s$,

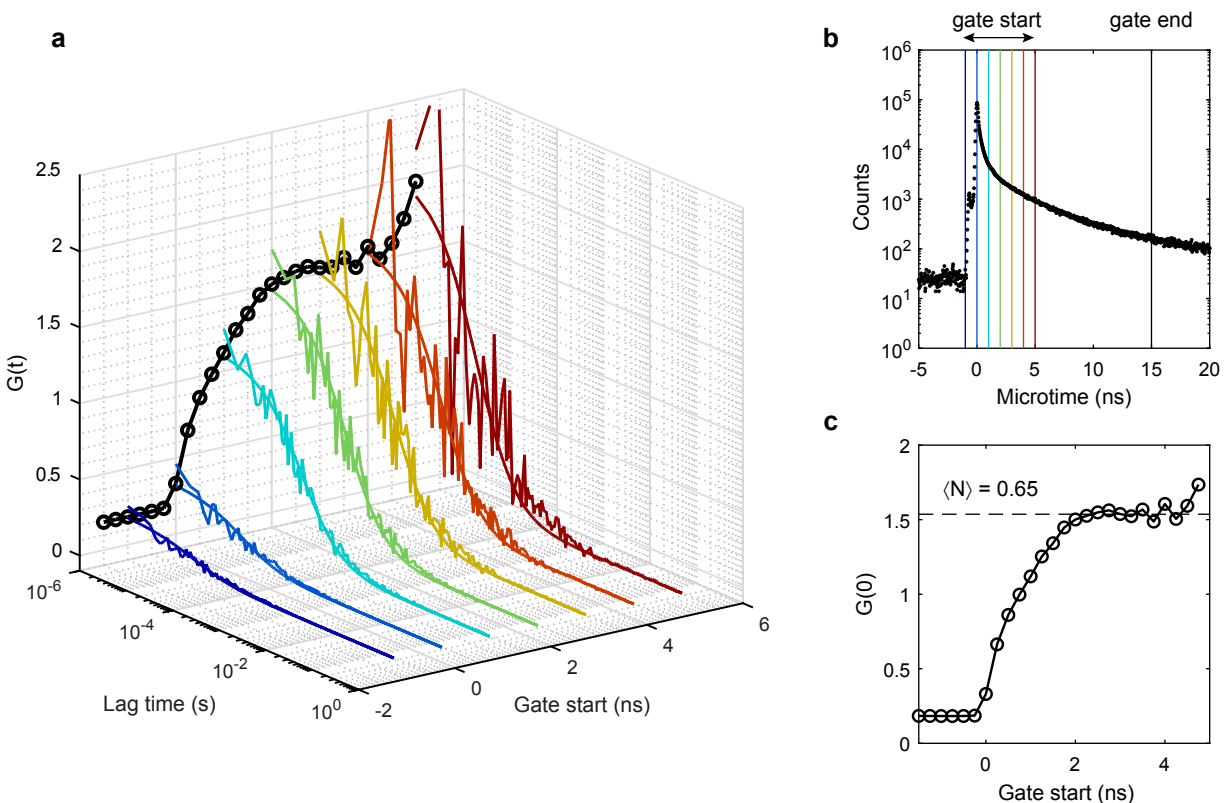


Figure S4: (a) FEIR-CS correlation functions from the 1 nM C6 solution as a function of the time gates displayed in (b). The early-time amplitude $G(0)$ is shown by black circles. (b) Time gates (color-coding matching to (a)) overlaid on the TCSPC histogram. (c) Early-time amplitude $G(0)$ as a function of the starting edge. The saturating value $G(0) = 1.54$ is indicated by a dashed line.

which is longer than that for the conventional FCS measurement on R6G in Figure S3b ($\tau_D = 32 \pm 2 \mu\text{s}$). Besides differences in molecular diffusion constant, the higher visible power used for the FEIR-CS measurement (26 pJ vs. 1.5 pJ) could result in a slightly larger effective probe volume if saturation effects are at play.¹¹

The 110 Hz FEIR count rate per molecule quoted in the main text was determined in part by considering the concentration dependence of the total photon count rate from the time series used for the FEIR-CS measurements, shown in Figure S5. The offset of the linear trend measures the non-molecular background B , while the slope of 78 Hz/nM, combined with the determination that $\langle N \rangle = 0.65$ at 1 nM, leads to 120 Hz per molecule ($F_1 + F_0$). Taking into account the B -free modulation ratio of 11 implies $F_1 = 110$ Hz. This number is also consistent with the 40 Hz F_1 level seen in Figures S2b and c considering that the visible excitation intensity used there is half that for the FEIR-CS measurements (12 pJ vs. 26 pJ).

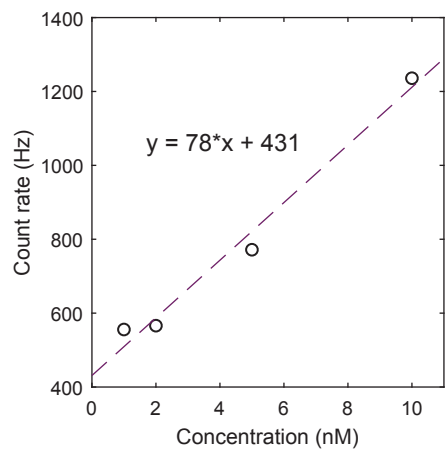


Figure S5: Concentration dependence of the total photon count rate for the time series underlying the FEIR-CS correlation functions (time gated to remove afterpulsing but not scattering). Linear trend shown by dashed line with equation.

5 Details of FEIR signal concentration dependence

The maximum FEIR signal F_1 and background level $F_0 + B$ shown in the concentration dependence in main text Figure 2a and reproduced here in Figure S6a were extracted from 1-IR-pulse measurements as indicated by the vertical arrows in main text Figure 1e. Time-gating was not used. The count rates were scaled by the variable visible excitation intensity (I_{vis} , average beam power divided by spot size) that was necessary to cover the 5 orders of magnitude in concentration C within the linear range of photon counting detection. The IR intensity was held constant (see Section S2). Implicit in this analysis is the linear dependence of the FEIR signal and one-photon background fluorescence on the visible intensity, which has been verified in ref. 1.

A small deviation from a linear trend (shown as dashed line in Figure S6a) for F_1 vs. C is more evident when also dividing through by C , which is plotted in Figure S6b. The value of $F_1/(CI_{\text{vis}})$, which should be constant for perfectly linear F_1 vs. C , decreases by factor of 2 from highest to lowest concentrations. This deviation is most likely due to overestimates of the true concentration in the lower range from accumulated systematic errors in the serial dilution procedure used to prepare the solutions and/or the sticking of dye molecules to interfaces.

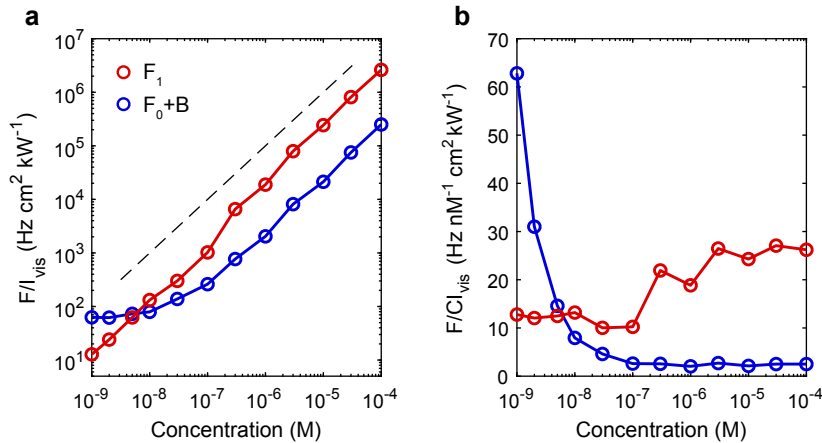


Figure S6: (a) C6 concentration dependence of F_1/I_{vis} (red circles) and $(F_0 + B)/I_{\text{vis}}$ (blue circles), reproduced from main text Figure 2a. The dashed line shows a linear dependence for reference. (b) Concentration dependence of $F_1/(CI_{\text{vis}})$ (red circles) and $(F_0 + B)/(CI_{\text{vis}})$ (blue circles).

References

- (1) Whaley-Mayda, L.; Penwell, S. B.; Tokmakoff, A. Fluorescence-Encoded Infrared Spectroscopy: Ultrafast Vibrational Spectroscopy on Small Ensembles of Molecules in Solution. *The Journal of Physical Chemistry Letters* **2019**, *10*, 1967–1972, DOI: 10.1021/acs.jpcllett.9b00748.
- (2) Giudice, A.; Ghioni, M.; Biasi, R.; Zappa, F.; Cova, S.; Maccagnani, P.; Gulinatti, A. High-rate photon counting and picosecond timing with silicon-SPAD based compact detector modules. *Journal of Modern Optics* **2007**, *54*, 225–237, DOI: 10.1080/09500340600763698.
- (3) Lakowicz, J., *Principles of Fluorescence Spectroscopy*, 3rd ed.; Springer US: 2006.
- (4) Wahl, M.; Gregor, I.; Patting, M.; Enderlein, J. Fast calculation of fluorescence correlation data with asynchronous time-correlated single-photon counting. *Opt. Express* **2003**, *11*, 3583–3591, DOI: 10.1364/OE.11.003583.
- (5) Enderlein, J.; Gregor, I. Using fluorescence lifetime for discriminating detector afterpulsing in fluorescence-correlation spectroscopy. *Review of Scientific Instruments* **2005**, *76*, 033102, DOI: 10.1063/1.1863399.
- (6) Widengren, J.; Mets, Ü. In *Single Molecule Detection in Solution*, Zander, C., Jorg, E., Keller, R. A., Eds.; Wiley-VCH Verlag GmbH & Co. KGaA: 2003; Chapter 3, pp 69–120.
- (7) Koppel, D. E. Statistical accuracy in fluorescence correlation spectroscopy. *Phys. Rev. A* **1974**, *10*, 1938–1945, DOI: 10.1103/PhysRevA.10.1938.
- (8) Hess, S. T.; Webb, W. W. Focal Volume Optics and Experimental Artifacts in Confocal Fluorescence Correlation Spectroscopy. *Biophysical Journal* **2002**, *83*, 2300–2317, DOI: [https://doi.org/10.1016/S0006-3495\(02\)73990-8](https://doi.org/10.1016/S0006-3495(02)73990-8).
- (9) Lamb, D. C.; Schenk, A.; Röcker, C.; Scalfi-Happ, C.; Nienhaus, G. U. Sensitivity Enhancement in Fluorescence Correlation Spectroscopy of Multiple Species Using Time-Gated Detection. *Biophysical Journal* **2000**, *79*, 1129–1138, DOI: [https://doi.org/10.1016/S0006-3495\(00\)76366-1](https://doi.org/10.1016/S0006-3495(00)76366-1).
- (10) Ghosh, A.; Karedla, N.; Thiele, J. C.; Gregor, I.; Enderlein, J. Fluorescence lifetime correlation spectroscopy: Basics and applications. *Methods* **2018**, *140-141*, Developments in Fluorescence Correlation Spectroscopy and related techniques, 32–39, DOI: <https://doi.org/10.1016/j.ymeth.2018.02.009>.
- (11) Enderlein, J.; Gregor, I.; Patra, D.; Dertinger, T.; Kaupp, U. B. Performance of Fluorescence Correlation Spectroscopy for Measuring Diffusion and Concentration. *ChemPhysChem* **2005**, *6*, 2324–2336, DOI: <https://doi.org/10.1002/cphc.200500414>.